ASME Journal of Tribology
Online journal at:
https://asmedigitalcollection.asme.org/tribology

Ruifeng Zhao
College of Mechanical and Electrical Engineering,
Nanjing University of Aeronautics and Astronautics,
29 Yudao Street,
Nanjing 210016, China
e-mail: zhaoruifeng@nuaa.edu.cn

Jie Ling[1]
College of Mechanical and Electrical Engineering,
Nanjing University of Aeronautics and Astronautics,
29 Yudao Street,
Nanjing 210016, China
e-mail: meejling@nuaa.edu.cn

Pengfei Zhou
College of Mechanical and Electrical Engineering,
Nanjing University of Aeronautics and Astronautics,
29 Yudao Street,
Nanjing 210016, China
e-mail: zhongjf@csu.edu.cn

Jianfeng Zhong
Hunan Aviation Powerplant Research Institute,
Aero Engine Corporation of China (AECC),
Zhuzhou 412002, China
e-mail: zhongjf@csu.edu.cn

Duan Yang
Hunan Aviation Powerplant Research Institute,
Aero Engine Corporation of China (AECC),
Zhuzhou 412002, China
e-mail: yangd892021@163.com

Analytical Modeling and Experimental Validation of Gear Churning Loss in Helicopter Transmission Lubrication Systems

Effective lubrication is essential for the helicopter transmission system to ensure smooth power transfer, reduce friction, and prevent overheating. However, churning loss caused by interactions between lubricating oil and rotating gears decreases efficiency, accelerates wear, and undermines system reliability. To enable quantitative analysis of gear churning loss, this article proposes an innovative fluid dynamics model targeting accuracy improvements for helicopter transmission compact gearboxes. The core idea is the mechanistic decomposition of total losses into drag and pocketing components, with explicit consideration of dynamic oil immersion depth and gearbox wall clearance effects. A custom-designed adjustable test platform for helicopter transmission gearboxes is developed to experimentally validate the model's predictive accuracy under diverse operating conditions, including rotational speeds ranging from 0 to 12,000 rpm and attitude angles of 0 deg, 10 deg, and 20 deg. Further investigations on the influence patterns of oil immersion depth and tooth width on gear pair churning loss are also conducted. Simulation results demonstrate that: (1) tooth width decisively determines loss mechanisms (end-face and pocketing losses contribute 46% and 10%, respectively, at 6 mm width, while end-face and pocketing losses contribute 10% and 74%, respectively, at 18 mm width) and (2) the evolution of dynamic oil surfaces with Froude number (Fr) causes variations in the immersion area, leading to overestimation of end-face losses. This work advances the design of lubrication systems by bridging theoretical predictions with experimental validation, offering actionable insights for reducing energy losses in high-performance transmissions.
[DOI: 10.1115/1.4069431]

Keywords: gearbox, churning loss, helicopter transmission, oil churning, oil pocketing, fluid friction, gears, stress intensity factors, surface layers, viscosity, wetting

1 Introduction

The transmission system, as the core of a helicopter, is tasked with efficiently transferring engine power to the main and tail rotors, ensuring the helicopter's lift and maneuverability. Without a reliable transmission system, the flight and precise control of a helicopter would be impossible. Therefore, the performance and safety of the transmission system directly determine the overall operational efficiency of the helicopter. Effective lubrication is essential for the helicopter transmission system to ensure smooth power transfer, reduce friction, and prevent overheating. However, churning loss caused by interactions between lubricating oil and rotating gears decreases efficiency, accelerates wear, and undermines system reliability. The critical importance of component longevity and reliable performance in demanding environments, whether in power transmissions or other mechanical systems, is a continuously explored area in engineering [1–3]. Understanding and mitigating these losses is therefore crucial for optimizing the design and operational lifespan of helicopter transmissions. Churning loss, the additional energy consumption resulting from the interaction between lubricating oil and moving parts, not only reduces the overall efficiency of the transmission system but can also lead to increased system temperatures, exacerbating wear on components such as gears. This, in turn, reduces the reliability and stability of the system, ultimately affecting the normal operation and maintenance cycle of the transmission system. Therefore, it is necessary to quantitatively study churning loss to improve the reliability of helicopter transmission system design, address issues of insufficient lubrication and excessive churning, and enhance the operational efficiency of the helicopter transmission system.

[1]Corresponding author.

Contributed by the Tribology Division of ASME for publication in the Journal of Tribology. Manuscript received April 30, 2025; final manuscript received August 6, 2025; published online September 8, 2025. Assoc. Editor: Robert L. Jackson.

Currently, the primary methods for studying gear churning loss include dimensional analysis based on experimental data, theoretical analysis based on fluid dynamics, and simulation analysis based on computational fluid dynamics (CFD).

As for the dimensional analysis based on experimental data, some early approaches were proposed. Terekhov [4] conducted extensive experiments on oil-immersed gearboxes, collecting data and establishing a dimensionless relationship between churning torque, Reynolds number (Re), and Froude number (Fr). Building on Terekhov's [4] work, Changenet and Velex [5] experimentally investigated the churning loss in automotive transmission gears and proposed a predictive formula based on dimensional analysis, considering factors such as speed, gear geometry, lubricant properties, and immersion depth. Later, they extended their research to study gear churning power loss under different flow regimes, introducing an extended formula that accounts for centrifugal effects, which was validated through experiments [6]. Chen and Matsumoto [7] developed a novel experimental platform with dual degrees of freedom to test the effects of gearbox spatial orientation and internal wall shape on splash-lubricated gear churning loss, proposing that these factors should be incorporated into churning loss modeling. Laruelle et al. [8] experimentally studied the churning torque of bevel gears under splash lubrication, analyzing the influence of gear structure and oil deflectors on dimensionless churning torque. Compared experimental results with model predictions from various literature, they identified discrepancies and highlighted the need for further validation of empirical formulas in predicting churning loss under the influence of oil deflectors. Quiban et al. [9] investigated the churning torque of spiral bevel gears under splash lubrication, observing that the churning torque initially reaches a local maximum, then a local minimum, and finally increases continuously at high speeds. This torque reduction phenomenon was linked to windage effects, leading to the proposal of a new load-independent loss prediction model.

In the absence of a complete understanding of the physical processes underlying churning phenomena, experimental analysis has played a crucial role in studying churning loss, laying a solid foundation for theoretical exploration of the underlying mechanisms. However, as research into churning phenomena has deepened, the limitations of experimental methods have become increasingly apparent, such as constraints on the applicability of gear structures and operating conditions, as well as the high costs associated with such studies.

With the rapid advancement of computer processing power, CFD technology has gradually become a crucial tool for solving nonlinear fluid problems. Particularly, the progress in rotor–stator interaction numerical simulation methods has made it feasible to use CFD for simulating the flow field during gear transmission processes. Mastrone et al. [10] proposed a numerical prediction method for gearbox lubricating oil flow and power loss based on the open-source CFD platform OPENFOAM®. They employed the dynamic mesh reconstruction method as the grid control strategy and innovatively validated the model's effectiveness in describing the oil-gas distribution within the gearbox using the PIV method. Additionally, the accuracy of the model in predicting load-independent losses of gear pairs was verified through torque measurements. Liu et al. [11] developed a CFD simulation model for a single-stage FZG gearbox under splash lubrication based on the finite volume method (FVM). By directly comparing the oil distribution and churning loss data obtained from the simulation with experimental results, they demonstrated the significant potential of CFD in predicting gear lubrication flow field characteristics and churning loss. Guo et al. [12] established a numerical simulation model for a spur/helical gearbox using the moving particle semi-implicit (MPS) method. The accuracy of the model was validated by comparing the simulated oil distribution and churning loss data with experimental results. Building on this, they further utilized the model to explore the impact of various factors on churning loss, providing valuable insights into the lubrication mechanisms of gearboxes. Hildebrand et al. [13] developed a CFD model for a single-stage gearbox that considered the shape of the gearbox inner walls and oil deflectors. After validating the model's accuracy through experiments, they investigated the mechanisms of churning loss and the influence of gearbox inner wall shapes and oil deflectors on churning loss. Liu et al. [14] established a simulation model consistent with Hildebrand's research [13] object using the MPS method. By comparing their results with the experimental data from Hildebrand's study [13], they verified the model's accuracy. Based on the model, they further analyzed the detailed effects of rotational speed, immersion depth, and oil deflector structural parameters on churning loss. Hu et al. [15] shifted their focus to spiral bevel gears, creating a CFD simulation model for a single-stage spiral bevel gear reducer. After validating the model's accuracy through experiments, they analyzed the mechanisms of churning loss and further explored the impact of oil deflectors on churning loss in single-stage spiral bevel gear reducers. Based on their findings, they proposed optimization strategies aimed at reducing churning loss. Concli et al. [16] focused on planetary reducers composed of multiple gears, establishing a lubrication flow field model for planetary gears using the dynamic mesh reconstruction method as the grid control strategy. They developed a power test bench for planetary gearboxes to validate the model and conducted a quantitative analysis of various power loss components in the planetary reducer based on the model. Ultimately, they emphasized that load-independent power losses account for a significant proportion of total losses in planetary reducers, warranting further research efforts.

Computational fluid dynamics simulation technology, when applied to analyze the physical processes of gear churning, can accurately capture the transient state of the flow field and provide rich physical field information. However, this analysis method incurs extremely high computational costs and demands significant computational resources and storage space. The convergence of flow field numerical solutions is sensitive to the quality of the mesh, mesh control strategies, and boundary condition initialization, necessitating multiple iterations of the mesh and solver.

Therefore, the hydrodynamic analytical model for gear churning loss presents advantages in this aspect, especially in situations where transient processes are not the focus. This model is capable of characterizing the churning power losses during the stable operation of a gearbox, requiring relatively low computational resources and time. Some scholars have provided precise descriptions of gear churning phenomena using mathematical language based on physical fluid dynamics theory. Diab et al. [17] established an approximate fluid dynamics model for the oil pumping phenomenon during the meshing process of spur/helical cylindrical gears. This model enables numerical solutions to the continuity equation for the volume change between gear teeth, revealing that the oil pump phenomenon is one of the key factors contributing to churning loss under high-speed rotation conditions. Seetharaman and Kahraman [18] and Seetharaman et al. [19] defined the load-independent loss of gears as the sum of drag loss caused by the interaction between a single gear and the fluid and the loss due to the pumping effect at the gear meshing interface. They developed predictive models for side/end face drag loss, root filling loss, and oil squeezing loss for a pair of meshing spur cylindrical gears. By comparing their results with experimental data on gear churning, they confirmed that the model could accurately predict rotational power loss. Following Seetharaman and Kahraman [18], Seetharaman et al. [19], Dai et al. [20], and Zhu and Dai [21] adopted their analytical approach for load-independent loss in spur cylindrical gears and conducted fluid dynamics theoretical analyses on the load-independent loss of single spiral bevel gears and orthogonal face gears under splash lubrication, respectively. They constructed predictive models that incorporated the structural parameters of the gears and validated the accuracy of these models through experiments, thereby expanding the application of fluid dynamics theory in predicting gear churning loss.

Theoretical analysis provides a precise mathematical representation of the complex physical process of gear churning, utilizing fundamental principles of fluid dynamics to explain the intricate mechanisms involved. This approach not only offers deep insights

into the nature of churning phenomena at very low computational costs but also effectively predicts churning loss. However, given the high level of physical and mathematical expertise required for theoretical analysis methods, their application in engineering practice remains relatively limited.

However, research reports on the modeling and prediction of compact gear pair churning loss in helicopter transmission systems remain relatively scarce. The important guiding significance of these studies in the engineering practices of forward design and optimization design for actual transmission systems has not yet been fully realized. Therefore, the motivation of this study is to construct a fluid dynamics-based analysis model for the churning loss of the accessory unit in a helicopter main reducer. This model aims to precisely quantify the impact of key system parameters on the churning power loss of a transmission system composed of multiple gears while ensuring high computational efficiency. To validate the accuracy of the simulation model, a test bench for measuring the churning torque of the helicopter main reducer accessory unit was designed and manufactured. Based on this test bench, the applicability and effectiveness of the model constructed in this study for predicting churning loss in transmission systems were verified. The contributions of this work lie in two aspects: (1) proposing a mathematical model for gear churning loss based on fluid dynamics, considering both the dynamic oil immersion depth and the clearance effects, and (2) presenting an experimental scheme for gear churning loss study with adjustable attitude angle to verify the analytical model.

The remainder of this article is arranged as follows. Section 2 elaborates on the methodology for constructing the gear churning loss model in this study. Section 3 presents the experimental components, including the test rig setup, experimental protocol, analysis of results, and model validation. Section 4 employs the established model to examine the influence of tooth width and oil immersion depth parameters on churning loss, along with an analysis of dynamic oil immersion depth and gearbox wall clearance effects. Finally, Section 5 summarizes the key research findings as conclusions.

2 Analytical Model

Research on gear churning loss presents multiple perspectives, with academic consensus on core mechanisms but differing emphases. Concli and Gorla [22] classified the losses from a gearbox system perspective into three categories: fundamental churning loss, meshing pumping losses, and bearing viscous dissipation, highlighting overall energy consumption characteristics. Stavytskyy et al. [23] focused specifically on the gear pair itself, proposing two core mechanisms—peripheral/side-face drag losses and thermal/pumping losses associated with the meshing zone—providing a simplified framework for localized analysis. Seetharaman and Kahraman [18] and Seetharaman et al. [19] advanced a five-component classification: further decomposing drag losses into peripheral drag, side-face drag, and tooth-space vortex losses, while separately quantifying meshing squeeze losses. This multiscale decomposition significantly enhances the prediction accuracy of churning loss.

Under oil-bath lubrication conditions, the interaction between rotating gear pairs and lubricating oil generates resistance to their movement. Based on the physical mechanisms of resistance formation, this can be broadly categorized into two types: drag loss caused by oil viscosity and pocketing loss resulting from oil pressure gradients. Consequently, the total churning loss of gear pairs can be expressed as

$$P_t = P_V + P_P \tag{1}$$

where P_V represents the drag loss due to oil viscosity, P_P denotes the pocketing loss caused by the pumping effect, and P_t signifies the total churning loss of the gear pair. The relative motion between partially submerged gear pairs and the oil, along with the viscous properties of the oil, are the primary causes of drag loss. The rotation of the gears drives oil flow, while the oil's viscosity exerts viscous friction resistance on the gears. To simplify calculations, this viscous friction resistance can be further divided into two components: circumferential loss acting on the gear's periphery and end-face loss acting on the gear's side surfaces. Thus, the drag loss can be expressed as

$$P_V = P_{dp} + P_{df} \tag{2}$$

where P_{dp} represents the circumferential drag loss of gear and P_{df} denotes the end-face drag loss of gear. In the meshing region of gear pairs, the periodic intrusion of gear teeth into the intertooth cavities induces a pumping effect. The resulting oil pocketing varies cyclically with the rotation angle of the gear pair, thereby hindering its motion.

Furthermore, to account for the influence of narrow clearances in compact gearboxes on drag losses, Eqs. (48) and (49) are introduced to quantify the effects of both axial and radial clearances on gear drag losses. Notably, the calculation formula for the gearbox wall clearance effect factor should be selected based on Re under specific operating conditions.

The analytical modeling of each churning loss component presented in this chapter is developed under the following fundamental assumptions:

(1) Incompressible viscous lubricant: Incompressible viscous fluid: The lubricating oil is treated as an incompressible Newtonian fluid, meaning its density remains constant while accounting for viscous effects.
(2) Isothermal flow condition: The system maintains constant temperature, resulting in temperature-independent lubricant viscosity.

2.1 Drag Power Losses. At high rotational speeds, the drag loss of gears can be approximated by modeling the gear as an equivalent cylinder with a tip radius. This simplification is justified because, under high-speed conditions, the gear tooth profile has a negligible influence on the boundary layer characteristics of the oil. Thus, the oil behavior around the gear pair primarily follows the interaction dynamics between a rotating submerged cylinder and the oil. Researchers such as Polly et al. [24] conducted experimental measurements of drag loss for individual spur gears, helical gears, and cylindrical gear blanks with identical tip diameters under varying immersion depths and rotational speeds. The study found that, under identical conditions, the drag loss of spur and helical gears was generally higher than that of cylindrical gear blanks. However, since drag loss constitutes a relatively small proportion of the total churning loss, this difference can be neglected in overall calculations. Subsequent experiments by Polly et al. [24] and colleagues on gear pairs further confirmed this observation.

2.1.1 Drag Loss on the Periphery. When modeling the gear as an equivalent disk, the interaction between the disk's periphery and the oil can approximate the actual gear-oil interaction. The viscous friction force on the disk's periphery can be abstracted as the integral of shear stress from planar plate flow within the boundary layer thickness over the submerged periphery. Assuming the lubricating oil is an incompressible fluid under steady flow conditions, the continuity equation [25] can be described as

$$\frac{\partial u_{rdp}}{\partial r} + \frac{u_{rdp}}{r} + \frac{1}{r}\left(\frac{\partial u_{\theta dp}}{\partial \theta}\right) = 0 \tag{3}$$

The Navier–Stokes equations [25] in polar coordinates are

$$\rho\left(\frac{\partial u_{rdp}}{\partial t} + \frac{u_{rdp}\partial u_{rdp}}{\partial r} + \frac{u_{\theta dp}\partial u_{rdp}}{r\partial \theta} - \frac{{u_{\theta dp}}^2}{r}\right) = -\frac{\partial P}{\partial r} + \frac{\mu}{r^2}\left(\frac{\partial^2 u_{rdp}}{\partial \theta^2} - u_{rdp} - \frac{2\partial u_{\theta dp}}{\partial \theta}\right) \tag{4}$$

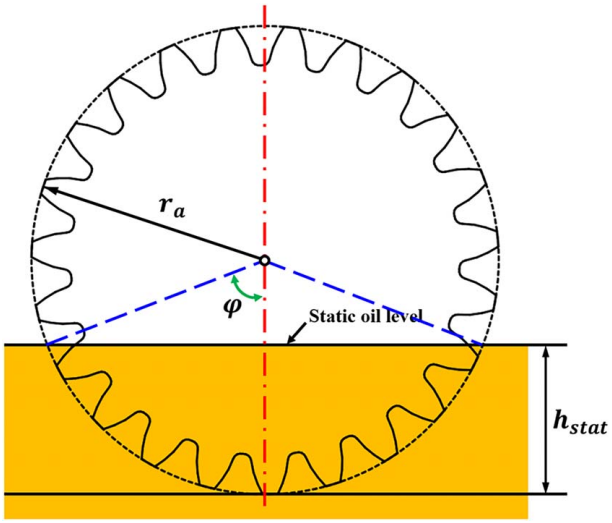

Fig. 1 Characteristic parameters of gear immersed in oil

$$\rho\left(\frac{\partial u_{\theta dp}}{\partial t}+\frac{u_{\theta dp}\partial u_{\theta dp}}{\partial r}+\frac{u_{rdp}u_{\theta dp}}{r}+\frac{u_{\theta dp}\partial u_{\theta dp}}{r\partial\theta}\right)=-\frac{\partial P}{r\partial\theta}+\frac{\mu}{r^2}\left(\frac{r^2\partial^2 u_{\theta dp}}{\partial r^2}+\frac{\partial^2 u_{\theta dp}}{\partial\theta^2}+\frac{r\partial u_{\theta dp}}{\partial r}+\frac{2\partial u_{rdp}}{\partial\theta}-u_{\theta dp}\right) \tag{5}$$

where ρ is the oil density and μ is the dynamic viscosity of the oil. Combining the continuity equation with the Navier–Stokes equations and applying the assumptions of incompressibility, steady flow, and planar plate flow yield

$$\frac{\partial u_{\theta dp}}{\partial\theta}=0 \tag{6}$$

$$\frac{\rho}{r}{u_{\theta dp}}^2=\frac{\partial P}{\partial r} \tag{7}$$

$$\frac{d^2u_{\theta dp}}{dr^2}+\frac{du_{\theta dp}}{rdr}-\frac{u_{\theta dp}}{r^2}=0 \tag{8}$$

Applying the no-slip boundary condition for the equivalent disk's peripheral velocity: $u_{\theta dp}=\omega\ r_a(r=r_a)$ and $u_{\theta dp}=0(r\to\infty)$, the solution is

$$u_{\theta dp}=\frac{\omega {r_a}^2}{r} \tag{9}$$

The viscous shear stress within the boundary layer is

$$\tau_{\theta dp}=\mu\left(\frac{r\partial\left(\frac{u_{\theta dp}}{r}\right)}{\partial r}+\frac{\partial u_{rdp}}{r\partial\theta}\right)=-\frac{2\mu\omega r_a^2}{r^2} \tag{10}$$

Thus, the viscous friction stress acting on the equivalent disk's periphery is $\tau_{wdp}=2\mu\omega$. Substituting this into the frictional resistance of the equivalent disk's periphery

$$F_{dp}=A_{dp}\tau_{\theta dp} \tag{11}$$

where A_{dp} is the submerged peripheral area of the equivalent disk as shown in Fig. 1. However, the interaction mechanism between gears and lubricating oil causes the free oil surface to exhibit dynamic evolution characteristics, thereby altering the oil-immersed area of gear disks. To accurately quantify the impact of this dynamic effect on circumferential losses, it is necessary to introduce Eq. (47) to calculate the dynamic oil immersion depth, thereby achieving quantitative characterization of the dynamic peripheral oil-immersed area:

$$A_{dp}=2\cos^{-1}\left(1-\left(\frac{h}{R_0}\right)_{dyn}\right)r_a b \tag{12}$$

where b is the tooth width of the gear.

The product of the resistance and the equivalent disk's peripheral linear velocity gives the circumferential drag power loss:

$$P_{dp}=F_{dp}\omega\, r_a \tag{13}$$

2.1.2 Drag Loss on the Face. Unlike the periphery, the gear's end faces exhibit significant velocity gradients along the radial direction, which may cause flow transition to turbulence. Laminar and turbulent flows exhibit distinct physical behaviors, necessitating Reynolds number Re calculations to determine the flow regime. The interaction between the equivalent disk's end face and the oil can still be treated as planar plate flow.

For laminar flow (Re <2000), the velocity distribution within the boundary layer [25] is linear.

$$u_{df}=\frac{Uy}{\delta} \tag{14}$$

where δ is the boundary layer thickness, U is the freestream velocity, $U=\omega\, r_a$, and y is the normal distance from the end face. The Skin friction coefficient [25] for the equivalent disk's end face is defined as

$$C=\frac{\tau_w}{\frac{1}{2}\rho U^2}=\frac{2\mu}{\rho U^2}\frac{du_{df}}{dy} \tag{15}$$

where τ_w is the wall shear stress. At $y=0$, $C=(2\mu/\delta\rho U)$. Using the von Kármán momentum integral equation, the boundary layer thickness [25] is

$$\delta=3.46\sqrt{\frac{\mu_k l}{U}} \tag{16}$$

where l is the length of the line segment connecting the two intersection points of the free surface and the gear tip circle. Substituting the boundary layer thickness into the friction coefficient

$$C=0.578\sqrt{\frac{\mu_k}{lU}} \tag{17}$$

where μ_k is the kinematic viscosity. The frictional resistance on the equivalent disk's end face is

$$F_{df}=\frac{1}{2}\rho\, U^2 A_{df} C \tag{18}$$

where A_{df} is the submerged area of one side of the equivalent disk's end face as shown in Fig. 1. Similar to the calculation of circumferential losses, Eq. (47) is introduced to quantify the dynamic oil immersion depth, thereby enabling precise characterization of the dynamic end-face oil-immersed area and its impact on end-face losses.

$$A_{df}={r_a}^2\left(\cos^{-1}\left(1-\left(\frac{h}{R_0}\right)_{dyn}\right)-\left(1-\left(\frac{h}{R_0}\right)_{dyn}\right)\sqrt{\left(\frac{h}{R_0}\right)_{dyn}\left(2-\left(\frac{h}{R_0}\right)_{dyn}\right)}\right) \tag{19}$$

The product of the resistance and the freestream velocity gives the end-face drag power loss

$$P_{df} = 2F_{df}U \tag{20}$$

For turbulent flow (Re >2000), the velocity distribution follows the one-seventh power law:

$$u_{df} = U\left(\frac{y}{\delta}\right)^{1/7} \tag{21}$$

Using the same method, the friction coefficient for the equivalent disk's end face is

$$C = 0.0276\left(\frac{\mu_k}{lU}\right)^{1/7} \tag{22}$$

The frictional resistance under turbulent flow is

$$F_{df} = \frac{1}{2}\rho U^2 A_{df} C \tag{23}$$

The end-face drag power loss is similarly calculated as

$$P_{df} = 2F_{df}U \tag{24}$$

2.2 Pocketing Loss. During gear meshing, the teeth of the driving and driven gears periodically intrude into each other's root gaps, causing a rapid reduction in the gap volume. This compresses the lubricating oil, forcing it to escape from both sides. Treating this periodically varying volume as a control volume, and given that gear pairs operate under continuous engagement ($\varepsilon > 1$), multiple control volumes coexist during rotation. The phase difference between successive control volumes is determined by the gear contact ratio. To calculate the pocketing power loss accurately, a model for the volume variation of a single control volume with rotation angle is first established. The analytical modeling of gear control volumes presents significant challenges, prompting the adoption of numerical discretization techniques to address their dynamic variations with rotation angle. In implementation, the angular range corresponding to a complete meshing cycle (from initial contact to final disengagement) of a single tooth is first uniformly discretized into N points, with each point representing a computational step. The normal cross-sectional area of the control volume is decomposed into three parts, as depicted in Fig. 2:

(1) The constant intertooth area A_1
(2) The time-varying area $A_{t2(n)}$ of the intruding tooth cross section
(3) The area $A_{b1(n)}$ enclosed by the nonmeshing tooth profiles of the driving and driven gears

The normal cross-sectional area of the control volume is

$$A_{C1(n)} = A_1 - A_{t2(n)} - A_{b1(n)} \tag{25}$$

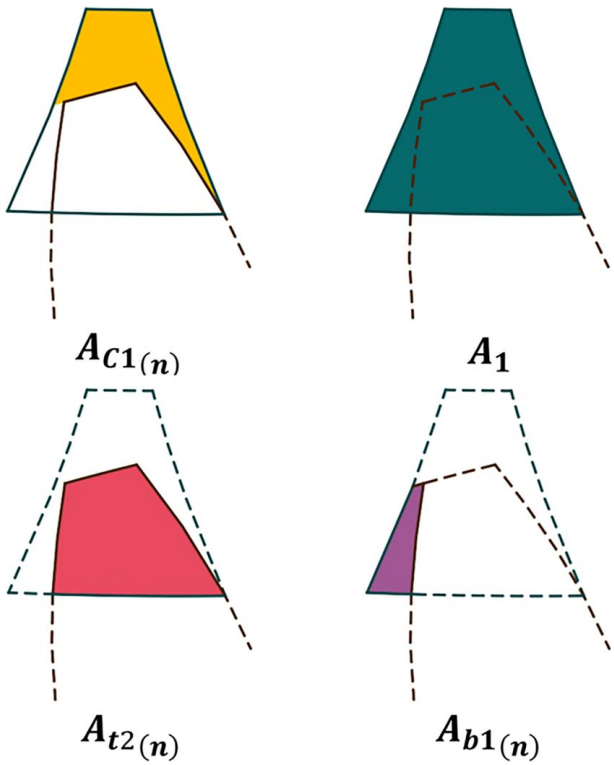

Fig. 2 Area segmentation at the *n*th computational step: $A_{C1(n)}$, A_1, $A_{t2(n)}$, $A_{b1(n)}$

To accurately compute the areas A_1, $A_{t2(n)}$, and $A_{b1(n)}$, further subdivision of these areas is required for computational tractability, as illustrated in Fig. 3. Here, $A1$ is defined as the region bounded by two adjacent involute tooth profiles of Gear 1, along with its base circle and tip circle. Since this area remains invariant during gear rotation, it can be treated as a constant and expressed as

$$A_1 = Q_{JO_1K} - Q_{JO_1M} - Q_{NO_1K} - Q_{MO_1N} \tag{26}$$

where Q_{JO_1K}, Q_{JO_1M}, Q_{NO_1K}, and Q_{MO_1N} represent the areas of subdivided geometric blocks, calculated as follows:

$$Q_{JO_1K} = \frac{r_{A1}}{2}\left(\frac{2\pi r_{a1}}{z_2} - s_{a1}\right) \tag{27}$$

$$Q_{MO_1N} = \frac{r_{b1}}{2}\left(\frac{2\pi r_{b1}}{z_2} - s_{b1}\right) \tag{28}$$

$$Q_{JO_1M} = \iint_{JO_1M} I_{inv1}(\theta)\, dr\, d\theta \tag{29}$$

where r_a1 and r_b1 represent the tip circle radius and base circle radius of Gear 1 respectively; z_1 denotes the number of teeth on Gear 1; s_a1 and s_b1 indicate the tooth thickness at the tip circle and base circle of Gear 1; $\mathrm{Iinv}_1(\theta)$ is the polar coordinate equation describing the involute tooth profile of Gear 1. For computational simplification, this is approximated using a first-order Taylor expansion: $I_{\mathrm{inv}1}(\theta) = r_{b1}\sqrt{1 + (3\theta)^{2/3}}$.

$A_{t2(n)}$ is defined as the area of Gear 2's tooth intrusion into Gear 1's tooth space, which varies with the rotation angle. It can be expressed as

$$A_{t2(n)} = Q_{FO_2E(n)} + Q_{EO_2D} + Q_{DO_2B(n)} - Q_{FO_2B(n)} \tag{30}$$

where $Q_{FO_2E(n)}$, Q_{EO_2D}, $Q_{DO_2B(n)}$, and $Q_{FO_2B(n)}$ represent the areas of subdivided geometric regions, calculated as follows:

$$Q_{FO_2E_{(n)}} = \iint_{FO_2E} I_{inv2}(\theta)\, dr\, d\theta \tag{31}$$

$$Q_{EO_2D} = \frac{1}{2}s_{A2}r_{a2} \tag{32}$$

$$Q_{DO_2B}(n) = \iint_{DO_2B} I_{inv2}(\theta)\, dr\, d\theta \tag{33}$$

$$Q_{FO_2B}(n) = \iint_{FO_2B} I_{A1}(\theta)\, dr\, d\theta \tag{34}$$

where r_{a2} denotes the tip circle radius of Gear 2; s_{a2} represents the tooth thickness at Gear 2's tip circle; and $I_{\mathrm{inv}2}(\theta)$ is the polar coordinate equation describing Gear 2's involute tooth profile, which is approximated using a first-order Taylor expansion for

computational simplification: $I_{inv2}(\theta) = r_{b2}\sqrt{1+(3\theta)^{2/3}}$ is Gear 2's base circle radius. Additionally, $I_{a1}(\theta)$ describes Gear 1's tip circle in the polar coordinate system with Gear 2's center as the pole: $I_{a1}(\theta) = a\cos\theta - \sqrt{{r_{a_1}}^2 - a^2\sin^2\theta}$, where a is the center distance between Gear 1 and Gear 2.

$A_{b1(n)}$ is defined as the variable area bounded by: one flank and tip circle of Gear 1 and one flank and tip circle of Gear 2, which changes with the rotation angle. It can be expressed as

$$A_{b1(n)} = Q_{JO_2G_{(n)}} - Q_{FO_2E_{(n)}} - Q_{JO_2F_{(n)}} \tag{35}$$

where $Q_{JO_2G_{(n)}}$ and $Q_{JO_2F_{(n)}}$ represent the areas of subdivided regions, calculated through:

$$Q_{JO_2G}(n) = \iint_{JO_2G} I_{A1}(\theta)\, dr\, d\theta \tag{36}$$

$$Q_{JO_2F}(n) = \iint_{JO_2F} I_{fit}(\theta)\, dr\, d\theta \tag{37}$$

where $I_{fit}(\theta)$ represents the fitted circular approximation of Gear 1's involute tooth profile in the polar coordinate system with Gear 2's center as the pole. Due to the mathematical complexity in deriving the exact involute profile equation in this coordinate system, we approximate it using a fitted circle expressed as: $I_{fit}(\theta) = e\cos\theta - \sqrt{{r_{fit}}^2 - e^2\sin^2\theta}$, where e is the offset distance between the fitted circle's center and Gear 2's center and r_{fit} is the radius of the fitted circle.

Once these areas are determined, the control volume's relationship with rotation angle is given by $V_{c(n)} = A_{C1(n)}b$. The integral form of the continuity equation for an arbitrary volume is

$$\frac{d}{dt}\int_V \rho\, dV = -\int_S \rho \boldsymbol{u} \bullet \boldsymbol{n}\, dS \tag{38}$$

Assuming incompressible, one-dimensional oil flow, the escape velocity is

$$u = -\frac{1}{A}\frac{dV}{dt} = -\frac{1}{A}\frac{dV}{d\theta}\omega \tag{39}$$

For a control volume with two leakage surfaces, the escape velocity is

$$u_{(n)} = \frac{1}{2A_{c(n)}}\frac{dV_{(n)}}{d\theta}\omega \tag{40}$$

Using Bernoulli's principle [25], the control volume pressure is

$$P_{(n+1)} = P_{(n)} + \frac{1}{2}\rho({u_{(n)}}^2 - {u_{(n+1)}}^2) \tag{41}$$

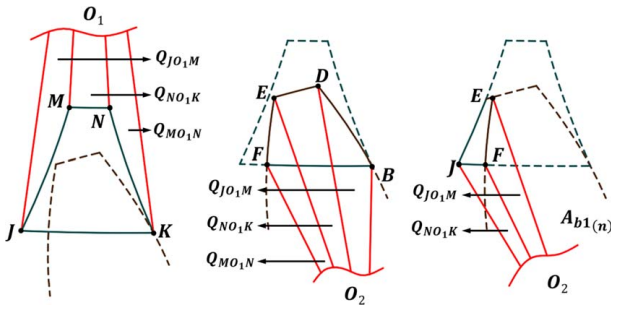

Fig. 3 Schematic diagram of area calculations for $A_{C1(n)}$, A_1, $A_{t2(n)}$, $A_{b1(n)}$ at the nth computational step

The resistance due to Pocketing is

$$F_{(n)} = \int_S P_{(n)} dA_{c(n)} = P_{(n)}A_{c(n)} \tag{42}$$

The pocketing power loss at the nth discrete angle is

$$P_{(n)} = F_{(n)}u_{(n)} \tag{43}$$

Averaging the losses over N discrete angles yields the time-averaged total pocketing power loss.

$$P_{p_{t-ave}} = \frac{1}{N}\sum_{n=1}^{N}\left(\sum_{i=1}^{V_{1(n)}} P_{p,1,i_{(n)}} + \sum_{i=1}^{V_{2(n)}} P_{p,2,i_{(n)}}\right) \tag{44}$$

where $P_{p_{t-ave}}$ represents the time-averaged squeezing loss of the gear pair, where $V_{1(n)}$ and $V_{2(n)}$ denote the number of control volumes for Gear 1 and Gear 2, respectively, at the nth computational step. Additionally, $P_{p,1,i_{(n)}}$ and $P_{p,2,i_{(n)}}$ correspond to the squeezing loss of the ith control volume for Gear 1 and Gear 2, respectively, at the nth computational step.

3 Experiments and Analysis

3.1 Test Platform Design. To validate the accuracy of the proposed model in characterizing gear churning loss, we developed a custom-designed adjustable test platform for aircraft gearbox churning loss analysis, as illustrated in Fig. 4. The test platform primarily consists of the following components: a custom-designed adjustable test rig, an electric motor, the test gearbox, torque sensors, couplings, and a control system.

The torque sensor, employed to measure power loss, is installed between the electric motor and the test gearbox. During testing, the gearbox operates under specified conditions, with the first-stage gearbox utilizing jet lubrication and the second-stage gearbox employing splash lubrication. In this process, losses due to oil jet lubrication and windage are neglected. Since no external load is applied to the gearbox, the input shaft is subjected solely to the resistance torque, enabling precise evaluation of the gearbox's churning loss.

Figure 4 shows the test transmission system mounted on the attitude-adjustable platform of the custom-designed adjustable test platform, which consists of an electric motor, an aircraft gearbox for testing, torque sensors, and couplings. The torque sensor is positioned between the input shaft of the test gearbox and the output shaft of the electric motor. It is connected to both shafts via diaphragm couplings, serving as an integral part of the drivetrain to transmit rotational speed and torque from the motor to the test gearbox. The experiments employed a Lanmec ZJ-50A torque-speed sensor with a measuring range of ±50 Nm torque and maximum rotational speed capability of 6000 rpm, featuring a high accuracy class of ±0.2% of full scale.

The test gearbox is designed with reference to the partial structure of a helicopter transmission system, simplified appropriately to create a two-stage gearbox test model. The first-stage gearbox consists of a pair of bevel gears configured for speed-increasing transmission, with a gear ratio of 0.487. It employs jet lubrication, and its associated losses are excluded from this study, as its primary function is to transmit motion to the second-stage gearbox.

The second-stage gearbox comprises a pair of cylindrical gears configured for speed-reducing transmission, with a gear ratio of 1.643. It utilizes oil-bath lubrication, and the driving gear's rotational speed is adjustable within a range of 0–12,000 rpm. Table 1 provides detailed specifications of the test gear pair.

The custom-designed adjustable test platform is constructed with three pairs of precision rotary joints. The rotation of these joints enables adjustment of the attitude angle of the test gearbox. The three-joint design is implemented to support the mass of the test platform and the test unit, thereby enhancing overall stability. After adjusting the joints to the predetermined orientation, spring-

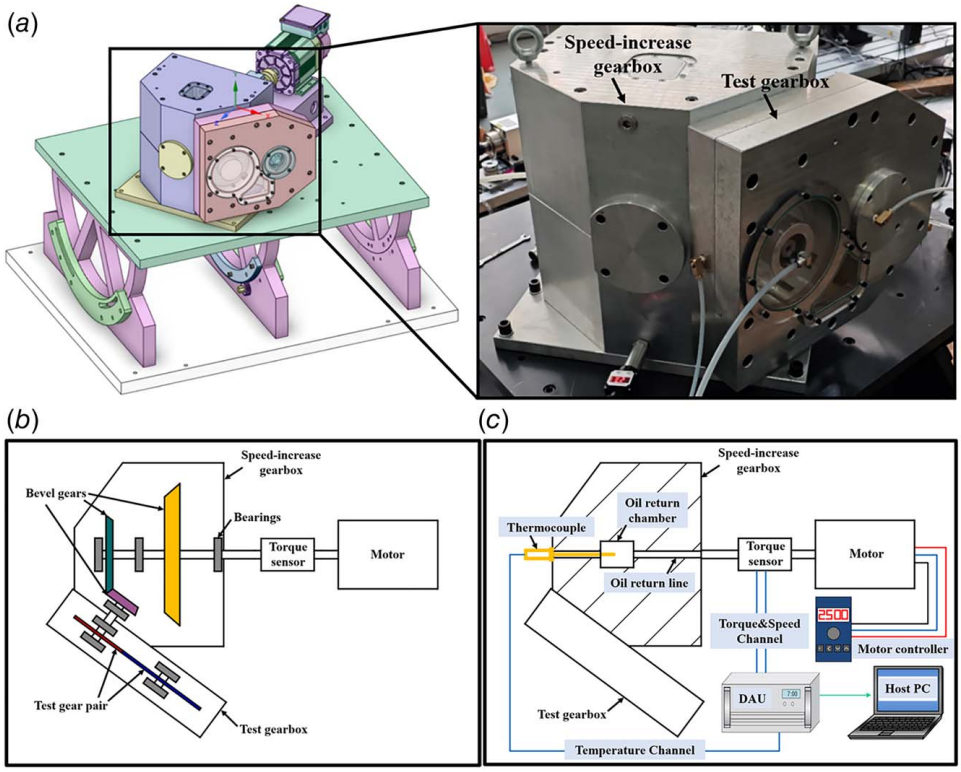

Fig. 4 Gear churning loss test system

Table 1 Characteristics of test gear pair

Parameters	Modulus (mm)	Number of teeth	Tooth width (mm)	Pressure angle (deg)	Center distance (mm)
Values	2.54	56/92	6.1	20	187.96

Table 2 Test conditions

Parameters	Rotational speed (rpm)	Pose angle (deg)	Kinematic viscosity (mm^2/s)	Density (kg/m^3)
Values	0–5700	0/10/20	61.64	853

loaded pins are engaged with positioning holes to lock the joints, ensuring precise and stable positioning of the test gearbox during operation.

3.2 Test Scheme. The torque data measured by the torque sensor can be decomposed into three primary components: drive system losses, gear friction losses, and churning loss. The first two components (drive system losses and gear friction losses) are closely related to the transmission system's load, primarily caused by contact friction in gears and bearings. In contrast, churning loss are independent of the transmission system's load. Under heavy-load and low-speed operating conditions, load-dependent power losses are comparable in magnitude to rotational power losses. However, as operational speed increases, the proportion of churning loss gradually surpasses that of load-dependent losses, eventually becoming the dominant factor in the total power loss.

Based on the aforementioned analysis and the research findings of Chen and Matsumoto [7], we can reasonably propose the following hypothesis: under extremely low-load conditions, both gear friction losses and drive system losses remain virtually constant regardless of variations in lubricant quantity.

Therefore, prior to conducting the formal test series, we first performed a set of calibration experiments under oil-free conditions to establish the baseline resistance torque T_0, which represents the combined effects of transmission system losses and gear friction losses at various rotational speeds. Subsequently, formal tests were conducted under specified oil immersion conditions to measure the total resistance torque T_1, encompassing transmission system losses, gear friction losses, and churning loss. Based on these measurements, the resistance torque attributable solely to churning loss can be calculated as

$$T = T_1 - T_0 \tag{45}$$

3.3 Experimental Results

3.3.1 Resistance Torque. Table 2 provides detailed test conditions.

To obtain reliable data for each test point, three sets of repeated measurements were conducted. Data acquisition was performed for 20 s after the torque stabilized, using a 100-Hz sampling rate to acquire 2000 raw data points per set. The acquired raw data underwent low-pass filtering to remove high-frequency noise, rigorous

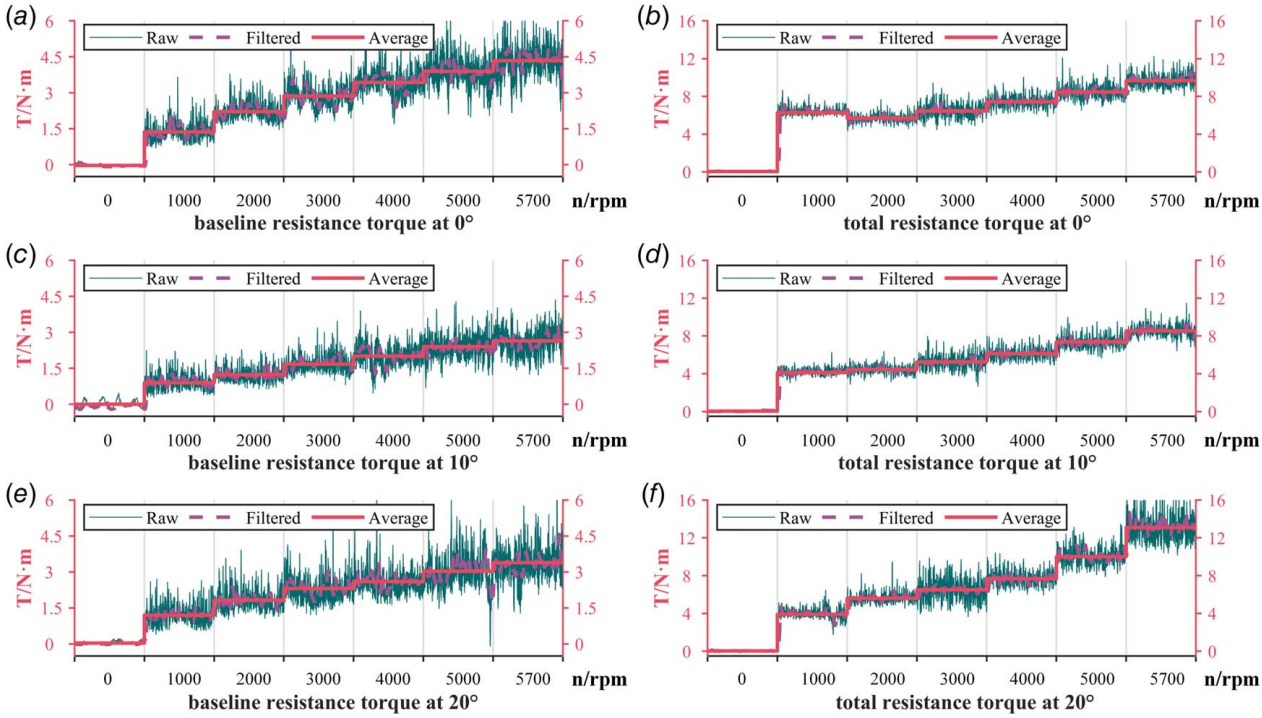

Fig. 5 The raw signals, filtered signals, and average values of total resistance torque and baseline resistance torque at 0 deg, 10 deg, and 20 deg

outlier removal, and finally, the mean was calculated, as illustrated in Fig. 5. The calculated mean was then subtracted by the zero-point offset of the torque sensor under static conditions, thereby determining the final measurement result for that test point.

Figure 6 illustrates the trends of the total resistance torque and baseline resistance torque of the test gearbox under different rotational speeds when the attitude adjustment mechanism is set at 0-deg, 10-deg, and 20-deg angles.

By comparing the stable baseline resistance torque under oil-free, no-load conditions across different attitude angles, it can be observed that the baseline resistance torque remains consistent without significant variations caused by changes in the attitude angle at all tested rotational speeds.

When comparing the total resistance torque data under full simulated oil volume at the same attitude angle, we observed an intriguing phenomenon: the resistance torque was consistently higher during acceleration (low-to-high speed) than during deceleration (high-to-low speed). Through controlled experiments with regulated oil tank temperature and the elimination of other potential factors, this discrepancy was confirmed to result from the lubricant's high sensitivity to temperature variations. In experiments without preheating, the total resistance torque measurements were lower than those obtained after preheating. However, when temperature was maintained constant, the resistance torque showed consistent values regardless of whether the speed was increasing or decreasing.

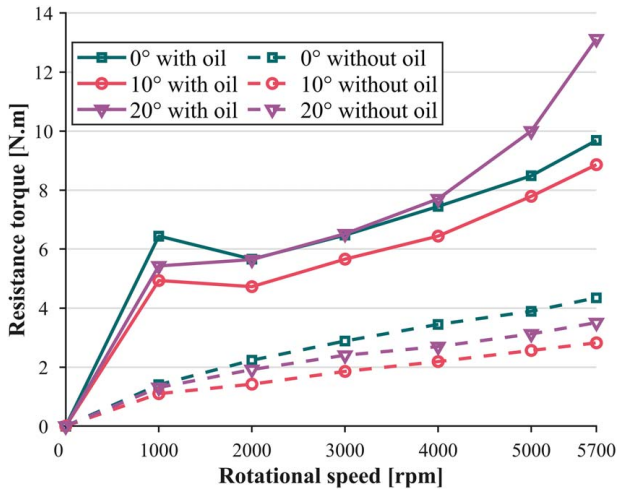

Fig. 6 Total resistance torque and baseline resistance torque at 0 deg, 10 deg, and 20 deg

When comparing the total steady-state resistance torque data under no-load conditions with full simulated oil volume at different attitude angles, we observed that the resistance torque initially increased with rotational speed until reaching a local maximum, followed by an anomalous decrease to a local minimum. Subsequently, the torque gradually rose again with further increases in speed. Quiban et al. [9] similarly noted this atypical decline in total resistance torque. Building upon LePrince et al.'s [26] research on gear splash flow, they revealed a significant correlation between gear immersion area and variations in total resistance torque, introducing the Fr to characterize the dynamic changes in the oil surface.

Notably, no significant differences were observed in the steady-state total resistance torque between 0-deg and 20-deg attitude angles. However, at a 20-deg attitude angle, the resistance torque remained consistent with the values at 0 deg and 10 deg when the rotational speed was below 2000 rpm. Once the speed exceeded 2000 rpm, the resistance torque generally became higher than that at 0 deg and 10 deg. This phenomenon can be attributed to gravitational effects hindering lubricant circulation, leading to an elevated stable oil level inside the gearbox.

3.3.2 Power Loss. Seetharaman et al. [18] and Seetharaman et al. [19] investigated the variation pattern of gear power loss with rotational speed under different oil level heights. This study, however, focuses on the variation pattern of power loss with rotational speed in the head casing and its accessory unit under different attitude angles. It is noteworthy that the attitude angle conditions

Table 3 Mapping table between attitude angle and oil immersion depth

Pose angle (deg)	Oil immersion depth $(h/R_0)_{stat}$
0	0.21
10	0.44
20	0.82

here can, to some extent, be regarded as a generalized concept of relative oil level height. Therefore, these two studies are essentially comparable. By comparing the variation pattern of power loss with rotational speed under different attitude angles in this experiment with the variation pattern of power loss under different relative oil level heights reported in the literature, we found that both exhibit consistent trends in how power loss changes with rotational speed. An increase in attitude angle is somewhat analogous to an increase in relative oil level height. As the attitude angle increases (equivalent to a rise in relative oil level height), the rate of power loss variation with rotational speed also increases accordingly—a phenomenon that aligns with findings reported in the literature.

However, this correlation between oil level and attitude angle largely depends on the structural design of the gearbox and cannot be directly quantified. Therefore, this study experimentally determined the oil level heights under different attitude angles, thereby refining and complementing the accuracy of the power loss analytical model.

Table 3 shows the experimentally determined static oil immersion height of the test gearbox gears when the attitude adjustment mechanism is positioned at 0 deg, 10 deg, and 20 deg, respectively.

The torque-speed data measured directly in the experiment only reflect the resistance characteristics at specific rotational speeds, which is insufficient to fully characterize the power loss. Therefore, to accurately evaluate churning loss, it is necessary to calculate the churning loss based on the churning resistance torque using the following formula:

$$P = \frac{Tn}{9550} \tag{46}$$

where P is the power loss (kW), T is the resistance torque (Nm), and n is the rotational speed (rpm).

Figure 7 demonstrates the variation trends of experimental power loss with rotational speed for the test gearbox under three distinct attitude angles (0 deg, 10 deg, and 20 deg) of the attitude adjustment mechanism. The total power loss exhibits a progressive increase with rising rotational speed. Notably, while the baseline power loss measurements show no significant differences across the 0-deg, 10-deg, and 2-deg conditions, the churning power loss component displays marked augmentation with increasing attitude angles.

3.3.3 Model Validation. Figure 8 shows the predicted and experimentally measured churning power loss in the test gearbox across different rotational speeds, with the attitude adjustment mechanism set at 0 deg, 10 deg, and 20 deg. The error bars on experimental data points represent the standard deviation among the mean values obtained from three independent measurement sets under each operating condition.

In the test gearbox, the churning power loss increases with the rotational speed of the driving gear, and the rate of power loss growth accelerates as the speed rises. It is noteworthy that the simulation results of the churning power loss model show good agreement with the experimental data. However, certain discrepancies exist between some simulation results and experimental data across different speed ranges. These deviations may stem from the complexity of the lubricating flow field in the test gearbox, where the interaction between the air-lubricant two-phase flow presents challenges for precise mathematical modeling. Additionally,

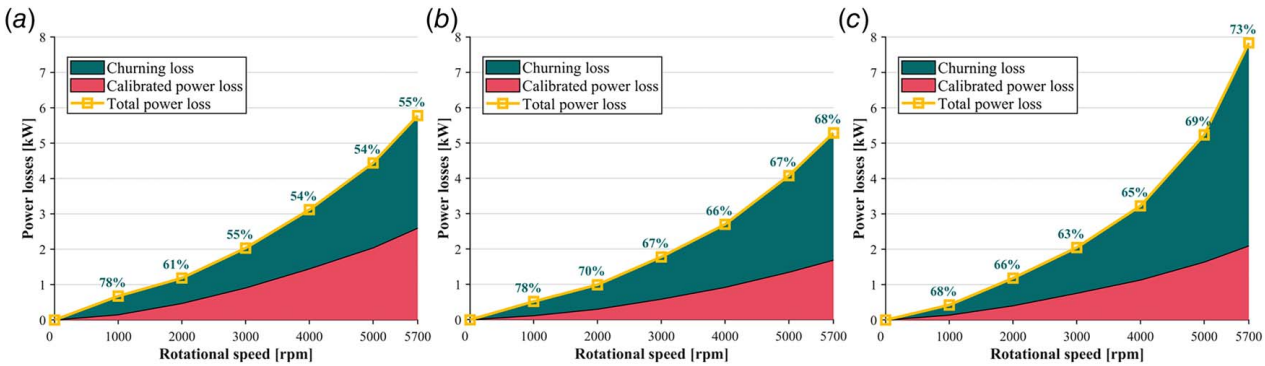

Fig. 7 Composition of power loss at 0 deg, 10 deg, and 20 deg

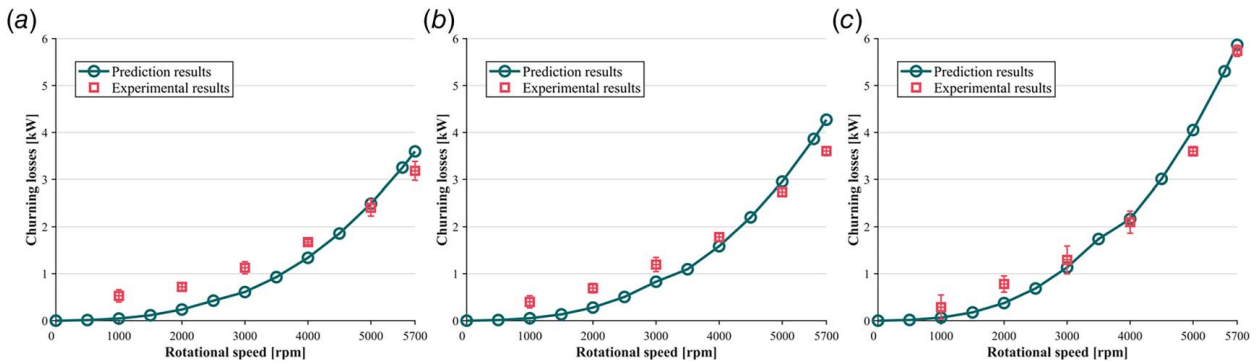

Fig. 8 Prediction and experimental results of churning power loss at 0 deg, 10 deg, and 20 deg

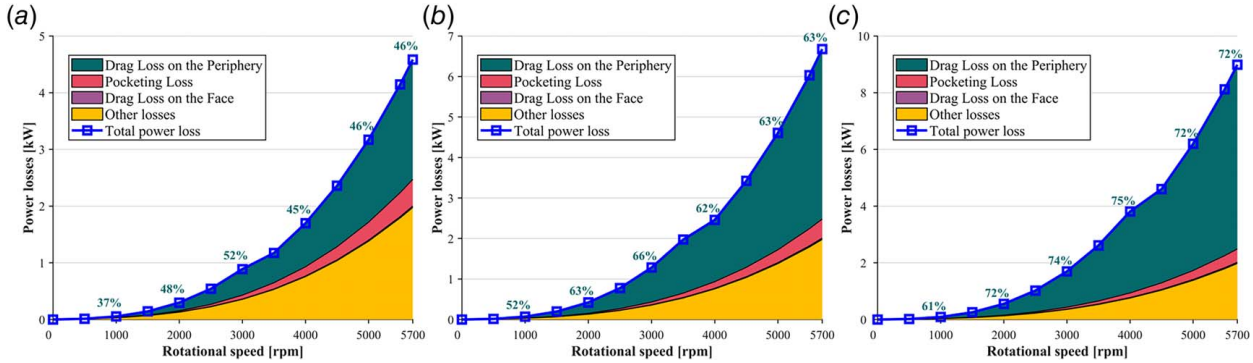

Fig. 9 Composition of churning power loss at $(h/R_0)_{stat} = 0.5$, $(h/R_0)_{stat} = 1.0$, and $(h/R_0)_{stat} = 1.5$

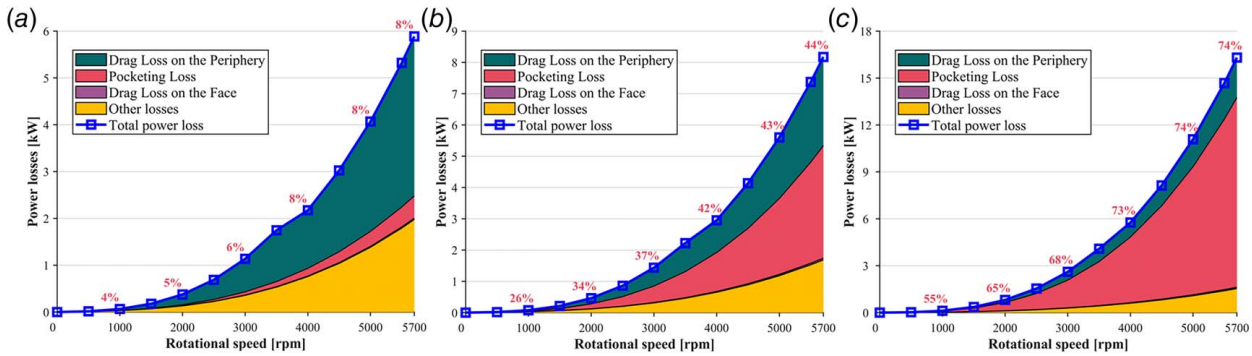

Fig. 10 Composition of churning power loss at $b = 6$ mm, $b = 12$ mm, and $b = 18$ mm

fluctuations in experimental results could be influenced by random errors in the testing environment and procedures.

Considering these factors, only deviations between predicted and measured values under high-speed conditions (rotational speeds ≥3000 rpm) were analyzed. The results demonstrate that at gearbox attitude angles of 0 deg, 10 deg, and 20 deg, the mean values of prediction deviation rates across different speeds were 20.4%, 16.1%, and 7.6%, respectively. Given that all prediction errors fall within acceptable thresholds, these results confirm the effectiveness and rationality of the proposed gear pair churning power loss model in characterizing actual churning loss.

4 Discussion

Building upon the confirmation that our model accurately characterizes gear pair churning power loss, we further employed it to analyze how gearbox design affects churning loss. Figure 9 illustrates the variation of churning loss with driving gear rotational speed at different oil immersion depths for identical gear pairs. In Fig. 9, the "other losses" category comprises both gear windage losses and bearing churning loss. These components were calculated using established engineering formulas: gear windage losses were determined through the Seetharaman [27] equation, while bearing churning loss were computed using the Harris [28] formula—with all calculations being performed under their respective operational conditions. Through comparative analysis of loss components across immersion depths, we identified that immersion depth primarily influences churning loss by altering end-face losses. Specifically, greater immersion depths correspond to larger wetted areas, thereby increasing the gear pair's circumferential losses.

Figure 10 shows the variation trend of churning loss of gear pairs with different tooth widths under the same oil immersion height as the driving wheel rotates. The "other losses" category shown in Fig. 10 maintains identical definition and scope to its counterpart in Fig. 9. By comparing the components of churning loss of gear pairs with different tooth widths under the same oil immersion height, we found that tooth width mainly changes churning loss by affecting pocketing loss and near-wall disturbance coefficients. Specifically, in the case of small tooth width ($b = 6$), the peripheral loss (46%) and pocketing loss (10%) contribute equally to the churning loss; while in the case of large tooth width ($b = 12$), the peripheral loss (25%) and the pocketing loss (44%) contribute equally to the churning loss; while in the case of large tooth width ($b = 18$), the peripheral loss (10%) and the pocketing loss (74%) contribute equally to the churning loss. A larger tooth width means an increase in the gear meshing volume and its rate of change over time, which further leads to an increase in squeezing pressure, thereby increasing the pocketing loss of the gear pair.

These relationship demonstrates how geometric parameters directly govern the dominant loss mechanisms in oil-immersed gear systems.

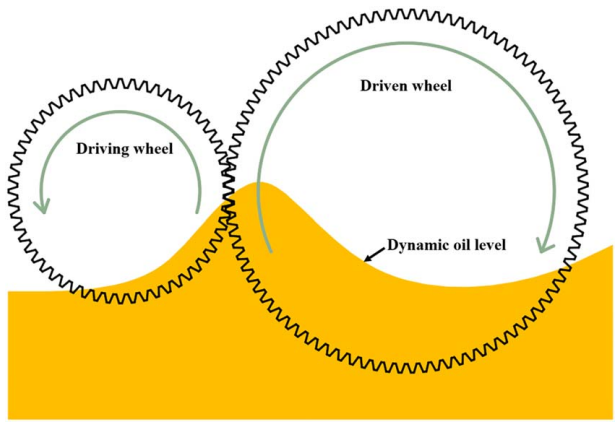

Fig. 11 Schematic representation of dynamic oil surface evolution

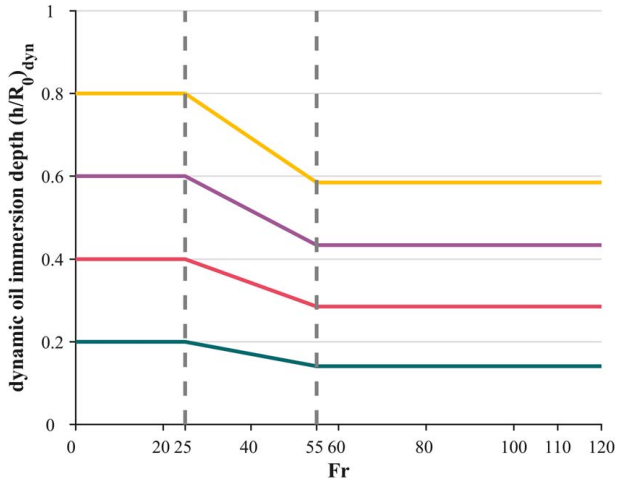

Fig. 12 Evolution trend of dynamic oil immersion depth with Fr

During experimental observations, the steady-state resistance torque exhibited a distinctive trend with increasing rotational speed: it initially rose progressively to reach a local maximum, then decreased to a local minimum, before monotonically increasing with further speed elevation. According to the theory proposed by Quiban et al. [9], this torque reduction phenomenon primarily stems from dynamic changes in the lubricating oil's free surface induced by gear motion. Figure 11 illustrates the schematic diagram of dynamic oil surface evolution. Due to the limited optical capabilities of our experimental setup, we were unable to directly capture the oil surface evolution phenomena illustrated in Fig. 11. However, the interfacial dynamics mechanisms described in Lucas et al.'s [29] work provide theoretical and experimental support for the oil surface behavior presented in our Fig. 11. The overestimation of end-face losses by static models stems from their fundamental assumption of fixed oil immersion depth, which presumes constant wetted area across all rotational speeds. This assumption fails to capture the actual speed-dependent variation in gear immersion area—the direct cause of loss overprediction. In reality, the free oil surface undergoes dynamic deformation under rotational forces, causing continuous changes in both immersion depth and wetted area. Notably, this dynamic oil surface effect on end-face losses becomes particularly pronounced in gear pairs with smaller tooth widths.

The dynamic deformation of the lubricant's free surface occurs when viscous forces transmit the rotational inertia of the gears to overcome gravitational effects, making this phenomenon quantifiable through the Fr—the dimensionless parameter characterizing the ratio of inertial to gravitational forces. Quiban et al.'s [9] theoretical framework further specifies three distinct regimes based on the Fr:

(1) When Fr <25: Gravitational forces dominate, and the free surface remains largely unaffected by gear rotation.
(2) When 25 ≤ Fr ≤ 55: Inertial forces begin to deform the free surface, creating a depression near the gear due to centrifugal effects that reduces the oil-immersed area as *Fr* increases.
(3) When Fr >55: The oil surface stabilizes in a dynamic equilibrium, showing negligible further changes despite increasing Fr values.

Considering the inherent complexity of gear-oil interactions, theoretical modeling of dynamic oil immersion depth presents significant challenges. Therefore, a hybrid approach combining physical modeling and experimental calibration was adopted using a semiinverse solution method. By establishing an empirical relationship between dynamic and static immersion depths through measured torque data, this method effectively bridges theoretical predictions with experimental observations. The approach successfully captures immersion depth variations caused by oil surface deformation while maintaining a balance between accuracy and practicality under limited computational resources.

$$\left(\frac{h}{R_0}\right)_{\text{dyn}} = \frac{\left(\frac{h}{R_0}\right)_{\text{stat}}}{-0.083\left(\frac{h}{R_0}\right)_{\text{stat}} + 1.435} \tag{47}$$

Figure 12 presents the relationship between the dynamic oil immersion depth and the Fr in this study.

The gearbox used in this study features a radial clearance of 0.6 mm and an axial clearance of 1.2 mm between the inner wall and gear pair. This specific geometry necessitates the incorporation of gearbox wall shape effects when modeling gear pair churning loss. Changenet and Velex [6] conducted extensive experimental investigations into how different flange and flow deflector configurations influence gear pair churning power loss. Based on their experimental findings, they proposed a churning loss factor to quantify the suppression effect of housing structure and side plates on gear churning loss.

At low-medium rotational speeds ($\text{Re}_c < 6000$):

$$\frac{P_{\text{ch}}}{P_{\text{ref}}} = \left(\frac{D_p}{D_f}\right)^{3/4} \left(\frac{j_a}{R_p}\right)^{0.383(D_p/D_f)} \tag{48}$$

At higher rotational speeds ($\text{Re}_c > 9000$):

$$\frac{P_{\text{ch}}}{P_{\text{ref}}} = 0.76\left(\frac{D_f}{D_p}\right)^{0.48} \left(\frac{j_a}{\sqrt{mb}}\right)^{0.548(D_p/D_f)} \tag{49}$$

where P_{ch} is the churning loss accounting for inner wall geometry effects, P_{ref} is the baseline churning loss without wall geometry considerations, D_p is the gear pitch diameter, D_f is the flange diameter, j_a is the axial clearance, and R_p is the pitch circle radius.

The model developed in this study incorporates Eqs. (48) and (49). For specific parameters: the pitch diameters of the driving and driven gears are set to $D_{P1} = 142.24$ mm and $D_{P2} = 233.68$ mm, respectively; their corresponding gearbox flange diameters are $D_{f1} = 148.52$ mm and $D_{f2} = 239.96$ mm; and the axial clearances between driving/driven gears and gearbox are both $j_{a1} = j_{a2} = 0.6$ mm. The baseline churning loss P_{ref} calculation, which excludes wall geometry effects, follows the methodology described in Sec. 2.1. Finally, the churning loss accounting for inner wall geometry effects P_{ch} has been integrated into the predictive content presented in Secs. 3.3.3 and 4.

Table 4 Comparative analysis with existing models

Metric	Proposed model	Jia et al. [30]	Liu et al. [11]	Shao et al. [14]
Modeling method	Analytical	Analytical	Finite volume method (FVM)	Moving particle semi-implicit method (MPS)
Predictive accuracy	<20%	<10%	10–30%	3.48–8.44%
Computational cost	<1 min	<1 min	8–10 h	94–174 h
Research object	Compact spur gear pairs	Single spur gears	Compact spur gear pairs	Compact spur gear pairs
Applicability	6000–12,000 rpm	500–5000 rpm	0–20 m/s	2–10 m/s

This study conducts a comparative analysis between the proposed model and several state-of-the-art models from recent literature, including but not limited to analytical modeling approaches, as well as CFD numerical methods encompassing both conventional FVM and the more innovative meshless MPS (moving particle simulation) method, as detailed in Table 4. The proposed model employs an analytical approach to predict churning loss in compact gearboxes, significantly reducing computational time compared to CFD methods while maintaining an acceptable level of prediction accuracy. Furthermore, compared with other analytical models, this study further incorporates the gearbox wall clearance effects and dynamic oil surfaces on churning loss, thereby significantly improving the prediction accuracy of gear pair churning loss under high-speed conditions.

5 Conclusions

To accurately characterize gear pair churning loss, a mathematical model was developed based on fundamental fluid dynamics principles. This model categorizes churning loss into two distinct physical mechanisms: drag losses and pocketing losses. The drag loss modeling incorporates two critical refinements—dynamic oil immersion depth and the effects of radial/axial clearances between gear pairs and gearbox walls—significantly enhancing the model's predictive accuracy for gear churning phenomena. Furthermore, in high-speed operational scenarios, a custom-designed adjustable test platform for aircraft gearbox churning loss analysis was designed and implemented to experimentally validate the proposed model. The study yielded the following key conclusions:

(1) The churning loss in gears can be fundamentally categorized into drag losses and pocketing losses based on their physical mechanisms. Drag losses originate from viscous friction between gears and lubricating oil, further subdivided into end-face losses and side-face losses according to the acting surfaces of viscous friction. Pocketing losses, on the other hand, result from the periodic volume changes between gear teeth that create pressure resistance against gear motion through lubricant compression.
(2) The analytical model proposed in this study serves as an effective tool for both calculating gear pair churning power losses and analyzing influencing factors, thereby providing valuable support for the forward design and improvement of aircraft transmission systems. Compared with existing churning loss prediction models, this study's formulation uniquely incorporates the effects of dynamic free oil surfaces and confined gearbox walls on churning loss.
(3) The immersion depth of lubricant significantly affects end-face losses. As the gear pair's Fr increases, the free surface of the lubricant undergoes dynamic changes that alter the effective immersion depth. To address this, a semi-inverse solution method was employed to establish the relationship between dynamic and static immersion depths. This advancement substantially refines the gear pair churning loss model, particularly enhancing its accuracy in high-speed operational scenarios.

However, it should be noted that the gear churning loss model established in this study does not account for the potential coupling relationship between the gearbox inner wall geometry and dynamic oil immersion depth, which represents a limitation of the current model. This could be the focus of future studies.

Conflict of Interest

There are no conflicts of interest.

Data Availability Statement

The authors attest that all data for this study are included in the article.

Nomenclature

a = Center distance
b = Tooth width
e = Offset distance between two centers
n = Rotational speed
u = Linear velocity
T = Torque
U = Freestream velocity
j_a = Axial clearance
r_a = Tip circle radius
r_b = Base circle radius
s_a = Tooth thickness at tip circle
s_b = Tooth thickness at base circle
A_c = Normal cross-sectional area of the control volume
A_{df} = End-face oil-immersed area
A_{dp} = Peripheral oil-immersed area
D_f = Flange diameter
P_{df} = End-face drag loss
P_{dp} = Circumferential drag loss
P_P = Pocketing loss
$P_{\mathrm{Pt-ave}}$ = Time-averaged pocketing loss
P_t = Drag loss
V_c = Control volume
Fr = Froude number
$(h/R_0)_{\mathrm{stat}}$ = Static relative immersion depth
$(h/R_0)_{\mathrm{dyn}}$ = Dynamic relative immersion depth
Re = Reynolds number
δ = Boundary layer thickness
μ = Dynamic viscosity
μ_k = Kinematic viscosity
ρ = X density
ω = Angular velocity

References

[1] Kumar, S., 2024, "Comprehensive Review on Role of Surface Modification Techniques to Prevent Failure of IC Engine Parts," Prot. Met. Phys. Chem Surf., **60**(2), pp. 218–269.
[2] Kumar, S., and Kumar, M., 2022, "Tribological and Mechanical Performance of Coatings on Piston to Avoid Failure—A Review," J. Fail. Anal. Prev., **22**(4), pp. 1346–1369.
[3] Kumar, S., Kumar, M., and Handa, A., 2018, "Combating Hot Corrosion of Boiler Tubes—A Study," Eng. Fail. Anal., **94**(12), pp. 379–395.
[4] Terekhov, A. S., 1975, "Hydraulic Losses in Gearboxes With Oil Immersion," Russ. Eng. J., **55**(5), pp. 7–11.
[5] Changenet, C., and Velex, P., 2007, "A Model for the Prediction of Churning Losses in Geared Transmissions—Preliminary Results," ASME J. Mech. Des., **129**(1), pp. 128–133.
[6] Changenet, C., and Velex, P., 2008, "Housing Influence on Churning Losses in Geared Transmissions," ASME J. Mech. Des., **130**(6), p. 062603.
[7] Chen, S.-W., and Matsumoto, S., 2016, "Influence of Relative Position of Gears and Casing Wall Shape of Gear Box on Churning Loss Under Splash Lubrication Condition—Some New Ideas," Tribol. Trans., **59**(6), pp. 993–1004.
[8] Laruelle, S., Fossier, C., Changenet, C., Ville, F., and Koechlin, S., 2017, "Experimental Investigations and Analysis on Churning Losses of Splash Lubricated Spiral Bevel Gears," Mech. Ind., **18**(4), p. 412.
[9] Quiban, R., Changenet, C., Marchesse, Y., Ville, F., and Belmonte, J., 2020, "Churning Losses of Spiral Bevel Gears at High Rotational Speed," Proc. Inst. Mech. Eng., Part J: J. Eng. Tribol., **234**(2), pp. 172–182.
[10] Mastrone, M. N., Hartono, E. A., Chernoray, V., and Concli, F., 2020, "Oil Distribution and Churning Losses of Gearboxes: Experimental and Numerical Analysis," Tribol. Int., **151**(11), p. 106496.
[11] Liu, H., Jurkschat, T., Lohner, T., and Stahl, K., 2017, "Determination of Oil Distribution and Churning Power Loss of Gearboxes by Finite Volume CFD Method," Tribol. Int., **109**(5), pp. 346–354.
[12] Guo, D., Chen, F., Liu, J., Wang, Y., and Wang, X., 2020, "Numerical Modeling of Churning Power Loss of Gear System Based on Moving Particle Method," Tribol. Trans., **63**(1), pp. 182–193.
[13] Hildebrand, L., Dangl, F., Sedlmair, M., Lohner, T., and Stahl, K., 2022, "CFD Analysis on the Oil Flow of a Gear Stage With Guide Plate," Forsch. Ingenieurwes., **86**(3), pp. 395–408.
[14] Liu, Y., Shao, S., Zhang, K., Yao, Y., and Wang, X., 2024, "Investigation of Characteristics of Splash Lubrication and Churning Power Loss in Gearboxes With a Guide Plate," Tribol. Int., **198**(8), p. 109875.
[15] Hu, S., Gong, W., and Gui, P., 2024, "Numerical Study on the Churning Power Loss of Spiral Bevel Gears at Splash Lubrication System," Lubr. Sci., **36**(4), pp. 259–276.

[16] Concli, F., Conrado, E., and Gorla, C., 2014, "Analysis of Power Losses in an Industrial Planetary Speed Reducer: Measurements and Computational Fluid Dynamics Calculations," Proc. Inst. Mech. Eng., Part J: J. Eng. Tribol., **228**(1), pp. 11–21.
[17] Diab, Y., Ville, F., Houjoh, H., Sainsot, P., and Velex, P., 2005, "Experimental and Numerical Investigations on the Air-Pumping Phenomenon in High-Speed Spur and Helical Gears," Proc. Inst. Mech. Eng., Part C: J. Mech. Eng. Sci., **219**(8), pp. 785–800.
[18] Seetharaman, S., and Kahraman, A., 2009, "Load-Independent Spin Power Losses of a Spur Gear Pair: Model Formulation," ASME J. Tribol., **131**(2), p. 022201.
[19] Seetharaman, S., Kahraman, A., Moorhead, M. D., and Petry-Johnson, T. T., 2009, "Oil Churning Power Losses of a Gear Pair: Experiments and Model Validation," ASME J. Tribol., **131**(2), p. 022202.
[20] Dai, Y., Ma, F., Zhu, X., and Ouyang, B., 2020, "Development of an Analytical Model to Estimate the Churning Power Losses of a Spiral Bevel Gear," Tribol. Int., **151**(11), p. 106536.
[21] Zhu, X., and Dai, Y., 2023, "Development of an Analytical Model to Predict the Churning Power Losses of an Orthogonal Face Gear," Eng. Sci. Technol. Int. J., **41**(5), p. 101383.
[22] Concli, F., and Gorla, C., 2014, "A CFD Analysis of the Oil Squeezing Power Losses of a Gear Pair," Int. J. Comput. Methods Exp. Meas., **2**(2), pp. 157–167.
[23] Stavytskyy, V., Nosko, P., Fil, P., Karpov, A., and Velychko, N., 2010, "Load-Independent Power Losses of Gear Systems: A Review," Teka Komisji Motoryzacji i Energetyki Rolnictwa, **10**(B), pp. 205–213.
[24] Polly, J., Talbot, D., Kahraman, A., Singh, A., and Xu, H., 2018, "An Experimental Investigation of Churning Power Losses of a Gearbox," ASME J. Tribol., **140**(3), p. 031102.
[25] Rubenstein, D. A., Yin, W., and Frame, M. D., 2022, "Chapter 2 – Fundamentals of Fluid Mechanics," *Biofluid Mechanics, 3rd ed., Biomedical Engineering*, D. A. Rubenstein, W. Yin, and M. D. Frame, eds., Academic Press, Amsterdam, The Netherlands, pp. 17–70.
[26] LePrince, G., Changenet, C., Ville, F., Velex, P., Dufau, C., and Jarnias, F., 2011, "Influence of Aerated Lubricants on Gear Churning Losses—An Engineering Model," Tribol. Trans., **54**(6), pp. 929–938.
[27] Seetharaman, S., 2009, "An Investigation of Load-Independent Power Losses of Gear Systems," Ph.D. thesis, The Ohio State University, Columbus, OH.
[28] Harris, T. A., and Kotzalas, M. N., 2006, *Advanced Concepts of Bearing Technology: Rolling Bearing Analysis*, CRC Press, Boca Raton, FL.
[29] Hildebrand, L., Liu, H., Paschold, C., Lohner, T., and Stahl, K., 2024, "Classification of Numerical, Experimental, and Analytical Approaches for Gearbox Oil Flow and No-Load Gear Power Loss," Eng. Sci. Technol. Int. J., **53**(5), p. 101661.
[30] Jia, F., Wang, B., and Fu, Y., 2024, "A Novel Prediction Model for Churning Power Loss of Spur Gear," Lubr. Sci., **36**(8), pp. 645–655.